JOURNAL OF MATERIALS SCIENCE **36** (2001) 2911 – 2924

Mechanical properties and shear failure surfaces for two alumina powders in triaxial compression

D. H. ZEUCH, J. M. GRAZIER, J. G. ARGÜELLO, K. G. EWSUK
Sandia National Laboratories, Albuquerque, NM 87185, USA
E-mail: dhzeuch@sandia.gov

In the manufacture of ceramic components, near-net-shape parts are commonly formed by uniaxially pressing granulated powders in rigid dies. Density gradients that are introduced into a powder compact during press-forming often increase the cost of manufacturing, and can degrade the performance and reliability of the finished part. Finite element method (FEM) modeling can be used to predict powder compaction response, and can provide insight into the causes of density gradients in green powder compacts; however, accurate numerical simulations require accurate material properties and realistic constitutive laws. To support an effort to implement an advanced cap plasticity model within the finite element framework to realistically simulate powder compaction, we have undertaken a project to directly measure as many of the requisite powder properties for modeling as possible. A soil mechanics approach has been refined and used to measure the pressure dependent properties of ceramic powders up to 68.9 MPa (10,000 psi). Due to the large strains associated with compacting low bulk density ceramic powders, a two-stage process was developed to accurately determine the pressure-density relationship of a ceramic powder in hydrostatic compression, and the properties of that same powder compact under deviatoric loading at the same specific pressures. Using this approach, the seven parameters that are required for application of a modified Drucker-Prager cap plasticity model were determined directly. The details of the experimental techniques used to obtain the modeling parameters and the results for two different granulated alumina powders are presented.

1. Introduction

Ceramic parts are commonly formed by uniaxially pressing granulated powders in rigid dies. During the press-forming process, the uniformity of the applied pressure throughout the compact ultimately determines the microstructural homogeneity of the green (i.e., unfired) body, and thus, is critical to near-net-shape forming. Because the relative density of a powder compact increases with increasing pressing pressure, variations in the applied pressure within a green body during powder compaction can contribute to density gradients in the compact after pressing. Such density gradients often increase the cost of ceramic component manufacturing and can degrade the performance and reliability of the finished part. Density gradients in green bodies manifest themselves as distortions in component shape after high-temperature firing, necessitating expensive hard grinding to obtain the desired final shape. More extreme gradients in density can contribute to defects in the form of laminations and cracks that deleteriously affect properties like tensile strength, and ultimately degrade the performance of the fired part. Severe density gradients can produce weak green bodies that either break during ejection from the forming die or that are too fragile to handle.

Historically, ceramic component manufacturers have relied heavily on trial-and-error to minimize density gradients in pressed powder compacts and to optimize processing. More recently, finite element method (FEM) modeling has been used to predict powder compaction response and to provide insight into the causes of density gradients in green powder compacts [1–9]. In addition to analyzing processing problems, numerical computer modeling technology also can be a powerful design tool that can be applied to optimize both component geometry and the pressing process (e.g., single- versus dual-action pressing) for a given powder before a single part is ever pressed [4, 5].

A critical component of any predictive model for powder compaction is the constitutive model that describes the mechanical behavior of the granulated powder. Continuum plasticity models, originally developed for applications in soil mechanics, can also be applied to ceramic powder compaction [3, 5–10]. In particular, Aydin *et al*. [2] have used a modified Drucker-Prager cap plasticity model within a finite element framework to model the compaction of granulated alumina powder during uniaxial die pressing. It is a constitutive model that is widely used in the field of soil mechanics to model compaction. As expressed in coordinates of the

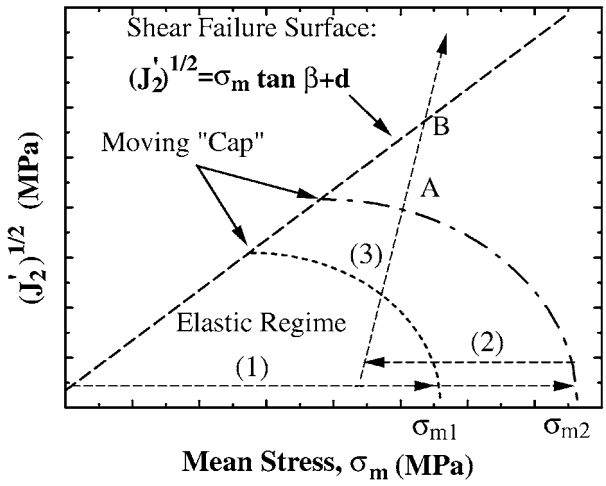

Figure 1 Illustration of the modified Drucker-Prager cap-plasticity model showing the shear failure surface and the cap. Loading within the wedge-shaped region defined by the shear failure surface, the cap, and the coordinate axes is elastic. The shear failure surface, which is defined by β (the angle of internal friction) and d (the material cohesion) is linear and fixed. The elliptical cap moves (hardens) with the application of increasing mean stress. Intersection of the load path with the shear failure surface defines the onset of permanent, plastic deformation by shearing. Intersection of the load path with the cap marks the onset of permanent, plastic deformation by a combination of shear and volumetric strain. Loading along the mean stress axis is in hydrostatic compression, and intersection with the cap produces permanent volumetric strain alone. In the load path examples shown, hydrostatic pressurization along the mean stress axis ($\sqrt{J_2'} = 0$) to σ_{m1} (dashed arrow 1) moves the cap such that it intersects the mean stress axis at (σ_{m1}, 0). Continued hydrostatic pressurization to σ_{m2} moves the cap irreversibly to the right where it intersects the mean stress axis at (σ_{m2}, 0). The shape of the cap can be probed by subsequently lowering the hydrostatic pressure to some arbitrary value of $\sigma_m < \sigma_{m2}$ (dashed arrow 2) and then loading the specimen deviatorically (dashed arrow 3). The response *should* be elastic until the cap is intersected at point A, and failure should occur at point B when the shear failure surface is intersected.

mean stress (σ_m) and the second invariant of the deviatoric stress ($\sqrt{J_2'}$), this model consists principally of two parts: (1) a linear shear failure surface showing increasing shear stress with increasing mean stress; and (2) a curved cap that intersects both the shear failure surface and the mean stress axis (Fig. 1).

Aydin *et al*. [2] indirectly measured most of the seven input parameters for the constitutive model in a single experiment that entailed die-pressing alumina powder at 89.6 MPa (13,000 psi). The remaining parameters for the model were estimated from data published in the open literature. The model was then implemented within the FEM framework, and its predictions were compared with results from an experiment used to determine the actual density gradients in a cylindrical alumina powder compact. Model predictions were generally in quite good agreement, though some discrepancies between the predicted and measured densities in the alumina compacts were noted. Aydin and co-workers [2] suggested that these were possibly a consequence of assuming that the angle of internal friction and cohesion were constant at all pressures and densities. Based on this reasonable agreement, Aydin *et al*. [2], concluded that the modified Drucker-Prager cap-plasticity model is applicable to ceramic powder compaction.

Clearly, numerical models for powder compaction can be valuable design and analysis tools; however, the predictions of any model will only ever be as good as the data used to run the simulation. A truly predictive model for powder compaction requires as inputs: (1) a representative constitutive model; (2) mechanical properties for the powder; and (3) the frictional properties of the powder in contact with the die.

As input, the modified Drucker-Prager cap-plasticity model requires seven material parameters including: bulk modulus (K), shear modulus (G), Young's modulus (E), Poisson's ratio (ν), angle of internal friction (β), cohesion (d), cap shape parameter (R), and transition surface parameter (α). However, ceramic powders, like soils and rock, are *pressure-sensitive* materials whose compressive strength and other mechanical properties depend on the ambient mean stress [11–13], so the material parameters should be known over the range of pressures used to press-form ceramic powders. The soil mechanics or geomechanics approach to obtaining the material properties of highly compressible soils has been to measure them directly using a combination of hydrostatic and triaxial (i.e., deviatoric loading) testing. However, soils are usually tested at quite modest pressures of typically a few hundred psi [12, 13]. With modifications in the experimental technique to account for the higher forming pressures and the larger strains in ceramic powder compaction, a similar approach to measuring material parameters for modeling should be applicable to ceramic powders.

Recently, we have undertaken an effort to implement an advanced cap-plasticity model for ceramic powders within the finite element framework [4–6]. The model is an extended Sandler-Rubin cap-plasticity model similar to that described by Sandler *et al*. [14]. Because representative numerical simulations require accurate material properties as well as realistic constitutive laws, an essential part of this effort has been to directly measure as many of the requisite powder properties for modeling as possible.

Based on the soil mechanics approach described, the objective of this work was to: (1) refine experimental techniques to characterize ceramic powders and determine the material parameters to apply to the extended Sandler-Rubin cap-plasticity model; (2) characterize the material properties and constitutive behavior of granulated ceramic pressing powders used in manufacturing; and (3) compare and contrast the results with those published in the open literature. This paper presents our experimental technique and the results of measurements to characterize the properties of two alumina powders. Details of the extended Sandler-Rubin constitutive model, and its numerical implementation in the FEM framework, are discussed elsewhere [4–6].

2. Materials

Two systems representative of granulated ceramic powders used in die pressing were characterized in this investigation, a 94% alumina and a 99.5% alumina powder. Both powders are specifically fabricated for, and are used to manufacture actual ceramic components by

die pressing. Typical of such powders used in ceramic manufacturing, both powders are comprised of nominally micrometer-size primary particles that have been granulated with organic binder through spray drying to produce nominally 100 micrometer agglomerates. After firing, the finished product is a debased alumina body comprised of alumina and a silicate-based glass phase. The 94% designation signifies that 94% of the inorganic matter present in the green powder is alumina, and 6% is glass. Additionally, both green powders contain several percent of organic matter, some of which is intentionally added as a binder to aid forming and to provide the compacted powder (tensile) strength after press forming. Theoretical green densities of 3.54 and 3.56 g/cc were calculated from the constituents for the 94% and 99.5% powders, respectively. These values were used to calculate the fractional densities discussed below.

3. Experimental techniques

The median agglomerate size, weight percent of organics lost on ignition, median primary particle size, and specific surface area of each powder were determined, as well as the density of a fully sintered body (i.e., 100% dense). Agglomerate size was measured using a commercial light scattering instrument (Horiba) with a dry powder feed attachment. Organic decomposition was characterized by heating 10 mg samples of the as-received alumina powder in flowing air at 10°C/min to 1000°C using a Perkin Elmer thermogravimetric analyzer (TGA). Samples for particle size and surface area analysis were prepared by first calcining the alumina powder (i.e., to remove the organic binder) by heating at 10°C/min to 700°C, and holding for 1 hr. After dispersing the calcined alumina powder in vacuum-degassed, deionized water with Darvan 7, particle size distribution was measured using a commercial light scattering instrument (Coulter LS230). A 5-point BET method for low surface area materials was used to measure the surface area of a 7–15 g sample of calcined alumina powder using nitrogen adsorption (Micromeritics 2010 ASAP). Prior to measuring specific surface, the calcined alumina was first degassed by heating at 115°C under vacuum overnight. Sintered density was determined on pulverized, sintered samples using He pycnometry (Quantachrome).

Hydrostatic and triaxial compression experiments were performed on the powders using a liquid-medium, triaxial testing cell [11, 12]. The cell consists of a cylindrical, 200 MPa (29,000 psi) pressure vessel with one end closure penetrated by a moveable piston (Fig. 2). The moveable piston permits application of a deviatoric load to a cylindrical test specimen, concurrent with a separately applied and controlled hydrostatic pressure. The cell is mounted in a servo-controlled, 978,600 N (220,000 lb) capacity MTS load frame that permits transfer of deviatoric load to the specimen. The triaxial cell is equipped with 12 coaxial electrical feed-throughs that permit direct strain measurements on specimens using various types of transducers, including standard foil strain gauges and, in this study, linear variable displacement transducers (LVDTs). Pressure was measured using a 207 MPa (30,000 psi) capacity pressure cell with a resolution of ±0.3 MPa (±45 psi). A 66,700 N (15,000 lb) capacity internal load cell having a resolution of ±169 N (±38 lb) was used to measure the deviatoric load applied to the specimen.

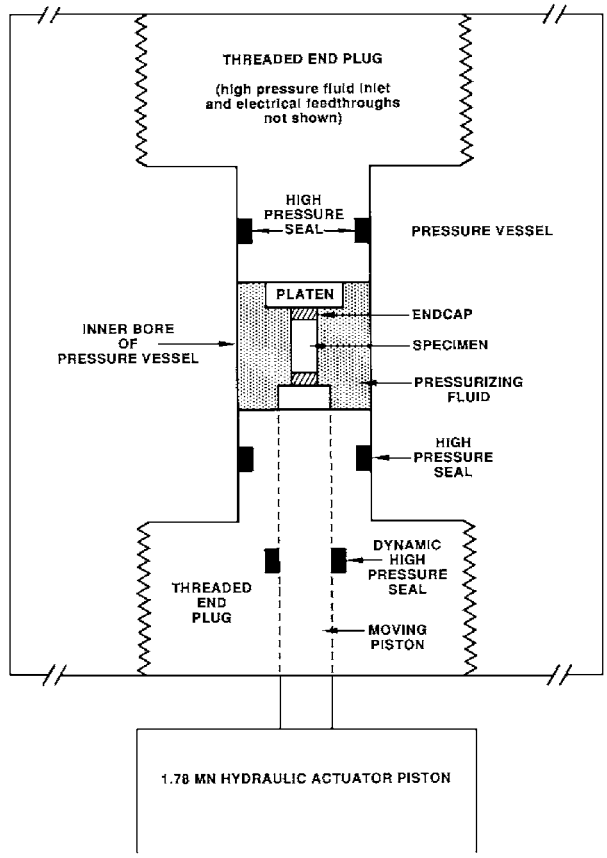

Figure 2 An illustration of the triaxial testing cell used in this study. A 978,604 N (220,000 lb) MTS test frame (not shown) transfers the load to the test specimen.

Signals from the load cell, pressure cell, and strain transducers were digitized and stored on hard disk using an IBM-compatible PC and the data acquisition program DATAVG [15]. Subsequent data reductions and the linear and nonlinear regressions described below were performed using PSI-Plot (Version 5), a commercially available data analysis and plotting software package.

Because loose ceramic powders have much higher porosity (i.e., approximately 65%) than soils and are ultimately pressed at much higher pressures, (e.g., in this case, 68.9 MPa or 10,000 psi), the strains are large, and the deformations are inhomogeneous, even under nominally hydrostatic compression. Deviatoric loading experiments at high pressures on such specimens would not be particularly meaningful because the initial state of the specimen (other than its density) would be ill-defined. For this reason, we refined the techniques used in soil mechanics to characterize ceramic powders. Experiments on the alumina powders were conducted in two separate test stages or series, which we will refer to as the hydrostatic and triaxial series. In the first series, the "raw" powders were compacted under a succession

of hydrostatic pressures to 68.9 MPa (10,000 psi) to: (1) establish a baseline pressure-density curve for each of the powders, and (2) create a suite of pre-compacted specimens of known density that would subsequently be used in the triaxial series. The specimen assembly consists of a cylindrical, 44.5 mm (1.75-inch) inner diameter by 133.4 mm (3-inch) long Viton jacket, sealed with two aluminum endcaps fitted with O-rings. One endcap is blind, while the other endcap is vented to the atmosphere via a long tube that penetrates the upper end closure. This testing configuration, in which gas is permitted to escape from the specimen, is referred to as the "drained" condition [11–13]. The vent tube is fitted with high pressure valves on *both sides* of the end closure (i.e., both inside and outside of the pressure vessel) for reasons that will be explained later. To prevent powder from being driven out of the specimen holder during pressurization, the vented endcap's port is covered by a disc of porous metal "felt", which allows air, but not the powder, to escape. To prepare the test specimen, the blind endcap is assembled to the rubber jacket and further held in place by plastic ties around the O-ring seal. A pre-weighed amount of powder is poured into the rubber jacket-endcap assembly, then vibrated for 60 seconds on the "low" setting using a Patterson Model V-1 dental vibrator. The vented endcap is then assembled to the rubber jacket, taking care not to exert undue force on the rubber jacket, and hence, the powder.

Repeated volume measurements were then made on the assembled specimen using Archimedes' method. The known volume of the jacket plus endcaps was subtracted out to determine the volume occupied by the powder. Powder weights are accurate to ± 0.01 g, and volume measurements on known standards are accurate and repeatable to ± 0.06 cm^3. Specimen-to-specimen variation in starting density for specimens prepared in this way is typically no more than ± 0.01 g cm^{-3}.

The assembled specimen is then loaded into the pressure vessel, and successively pressurized to several different pressures, for example, 3.5, 6.9, 13.8, 20.7, 27.6, and 34.5 MPa (500, 1000, 2000, 3000, 4000 and 5000 psi, respectively). For the hydrostatic tests, the movable piston is kept locked in place, and out of contact with the specimens. At the top of each pressurization stage, a vacuum is applied to the specimen from *outside* the pressure vessel, the pressure is reduced to atmospheric, and the sample is removed from the vessel after valving the specimen off using the valve located *inside* the pressure vessel. In this way, a vacuum is maintained on the now-compacted specimen, and the jacket remains compressed tightly against the powder.

Repeated volume measurements are then performed on the compacted specimen, and a density corresponding to that particular pressure is determined. The sample is then returned to the pressure vessel, the valves are opened, and the specimen is pressurized to the next value in the series. The specimen is thus repeatedly pressurized, removed, measured, and re-pressurized until the final, or *target* pressure is reached, 34.5 MPa (5000 psi) in our example above. Typically, our target pressures were 6.9, 20.7, 34.5, 51.7, and 68.9 MPa (1000, 3000, 5000, 7500 or 10,000 psi, respectively). In this way, we determined the pressure-density curves for the alumina powders up to 68.9 MPa (10,000 psi), and also obtained a suite of pre-compacted specimens of known density that could be machined into cylinders of known length and diameter for subsequent triaxial testing at the various target pressures up to 68.9 MPa (10,000 psi).

Note that because the volume strain and density measurements are performed at atmospheric pressure, elastic contributions to the volume strain and hence, density, have been ignored in the plots that we present. Volumes at pressure are actually slightly smaller than those measured, and densities at pressure would be correspondingly higher. However, based on calculations using the bulk moduli that we measured at the target pressures, these contributions should comprise only 2 to 3% of the measured plastic strain at the pressures we have investigated. As such, we feel that it is reasonable to ignore the elastic contribution at this time. Note that we are also assuming that repeated removal from the pressure vessel does no damage to the specimens prior to the volumetric measurements. Because we: (1) do not remove the rubber jacket to make the several volume measurements; (2) maintain a tight vacuum on the sample before and during removal of the specimen from the pressure vessel; and (3) handle the specimen with great care while performing the volume measurements, we believe that this is a sound assumption. The repeatability of our measurements supports this assumption.

For triaxial testing, an intermediate machining step was necessary because frictional constraints at the endcaps resulted in inhomogeneous compaction. The decrease in diameter was greatest in the central region of the specimen and least immediately adjacent to the endcaps. Meaningful stress and strain measurements during the deviatoric loading stage would have been impossible without accurate starting measurements of the specimens' lengths, diameters and cross-sectional areas. Therefore, the isopressed compacts were gently turned on a lathe down to right circular cylinders having a diameter of 25.4 mm (1 in), and the ends were carefully ground perpendicular to the cylinder axes. A specimen length-to-diameter ratio of 2:1 was maintained in all cases.

The machined specimens were weighed, and a "geometric" density was calculated using the specimen dimensions. These values typically agreed to within 2–3% with the values determined using Archimedes' method, and were performed only to confirm that the machining had not caused any serious changes in the condition of the specimens.

In some cases, weaker specimens prepared at the lower pressures experienced some edge chipping during handling. Prior to testing these specimens, the chips were filled with soft, silicone rubber caulking.

The now-cylindrical specimens were placed inside a jacket of shrink-to-fit polyolefin tubing, sealed on top and bottom with endcaps, and the tubing was heat-shrunk around the specimen and endcaps. Again, the lower endcap was vented to the atmosphere. The endcaps were equipped with holders for a pair of

diametrically opposed LVDTs to measure axial strain. A single spring-loaded LVDT held in a clip-on fixture measured diametral strain. Displacement measurements in the axial and diametral directions are resolvable to 0.025 and 0.0152 mm (0.001 and 0.0006 in), respectively.

The instrumented assembly was then returned to the triaxial test cell, and pressurized back to the target pressure (viz., the highest confining pressure that the specimen experienced during hydrostatic compression). Axial and lateral strains were monitored during this period and exhibited varying degrees of anisotropy. Once the target pressure was reached, a depressurization-pressurization loop or cycle was performed to measure the bulk modulus of the specimen. This is a standard technique used to measure the elastic moduli of soils and other granular materials under particular conditions of pressure, stress, and void space [12]. The absolute magnitude of the pressure cycle depended on the target pressure, with larger loops possible at the higher pressures. However, to preserve the original state of the specimen, it is never completely depressurized during the cycle.

Volumetric strains that were measured during the re-pressurization were typically quite a bit larger than the elastic strains predicted from the bulk moduli (see below) measured at the target pressures: 0.03-0.037 vs. 0.007, respectively, at 6.9 MPa (1000 psi), and 0.045–0.065 vs. 0.008, respectively, at 68.9 MPa (10,000 psi). Measured strains were also quite nonlinear. These results suggest that we did indeed do some slight damage to the specimens during final unloading, jacket removal, machining, and triaxial specimen assembly. However, by monitoring the sample strains during repressurization to the target pressure, we believe that we were able to correct for this once the target pressure was reached, assuming homogeneous deformation.

Up to this point, the specimen has been subjected only to hydrostatic pressure. Now, the moveable piston is slowly moved into contact with the specimen endcap as indicated by slight increases in load and axial strain. The piston movement is briefly halted, and then resumed at a constant displacement rate corresponding to a nominal axial strain rate of 1×10^{-4} s^{-1}. During the course of the axial deformation, the specimen was partially unloaded and reloaded periodically to measure Young's modulus and Poisson's ratio [12]. Again, the magnitude of the unloading/reloading cycle depended upon the confining pressure and strength of the specimen. Deformation continued until either maximum load cell capacity of 66.7 kN (15,000 lbs) was reached, or until we approached the maximum travel of the diametrical LVDT of 6.35 mm (0.25 in). We inevitably ran out of diametral LVDT travel before we ran out of axial LVDT travel, 12.7 mm (0.5 in). Pronounced "barreling" of the specimens was observed under all test conditions, and axial stresses were continuously corrected for the change in cross-sectional area.

In our discussions below, σ_1, σ_2 and σ_3 are the greatest, intermediate, and least principal stresses, respectively, with compression reckoned positive. In our triaxial compression experiments, σ_1 is applied parallel to the cylindrical axis of the test specimens via the moveable piston, and $\sigma_2 = \sigma_3 =$ the fluid pressure. For triaxial tests, we will also frequently refer to σ_3 as the *confining pressure*. In our hydrostatic compression experiments, of course, $\sigma_1 = \sigma_2 = \sigma_3$, and we may occasionally refer to the fluid pressure simply as P when discussing hydrostatic tests.

4. Results and discussion

4.1. Powder properties and characteristics

The physical properties and physical characteristics of the 94% and 99.5% alumina powder systems examined in this study are presented in Table I. From the results presented, the two powder systems are similar in that both are high-alumina bodies with sintered densities approaching that of pure alumina (i.e., 3.99 g/cc), and both are comprised of roughly 115 μm median size agglomerates. However, there appear to be considerably more differences between the two powders than similarities. In addition to the obvious fact that the 99.5% alumina body contains less second-phase glass, the TGA organic burnout results reveal that it also contains more organics than the 94% alumina powder. Additionally, based on the fact that the burnout profiles are different for the two powders, it can be concluded that the organics present (i.e., including the organic binder) are not the same in both systems. The primary particles that make up the two different powders appear to be significantly different as well. The higher specific surface area and smaller median particle size measured for the 99.5% alumina powder system indicate that it has a finer particle size than the 94% alumina powder system.

In general, the compaction behavior and the mechanical properties of a pressing powder system are expected to be influenced by the physical properties and physical characteristics of that powder system. While it is not possible to systematically examine such relationships in the industrial powders characterized in this study, some of the similarities and differences determined for the 94 and 99.5% alumina powder systems may provide some insight into the possible influence of powder characteristics on powder compaction. Furthermore, such insight could be invaluable in designing and conducting more systematic experiments to discern relationships between powder characteristics and compaction behavior, possibly by designing and fabricating new powder systems that may not necessarily be characteristic of the powders currently used in the manufacturing environment.

TABLE I Summary of the alumina powder physical properties and physical characteristics

Powder	Organics Lost On Ignition (wt.%)	Median Agglomerate Size (μm)	Median Particle Size (μm)	Specific Surface Area (m^2/g)	Sintered Powder Density (g/cc)
94% Alumina	4.4	113	4.2	$1.85 \pm .03$	3.87
99.5% Alumina	5.5	122	2.0	$3.20 \pm .03$	3.97

4.2. Hydrostatic compression

Plots of pressure versus volume strain and fractional density versus pressure for the 94% and 99.5% alumina powders are shown in Fig. 3a and b, respectively. Fig. 3a shows that the 99.5% alumina consistently exhibits less volume strain than the 94% powder at all pressures above 20.7 MPa (3000 psi). Additionally, the 99.5% powder initially packs to a higher fractional green density, and compacts to higher densities over the entire pressure range studied (Fig. 3b).

The difference in compaction response under nominally hydrostatic conditions represents a distinct difference in behavior between the two powders. This difference was also readily apparent in specimen preparation. In contrast to the 94% alumina, for which specimens were formed at pressures as low as 3.5 MPa (500 psi), it was impossible to fabricate triaxial test specimens from the 99.5% alumina powder at pressures below 20.7 MPa (3000 psi). Pressed billets either fell apart during removal from the Viton jacket, or during the machining operation. Even those specimens pressed at 20.7 MPa (3000 psi) experienced some minor chipping at the ends during machining. Thus, the material that exhibited the least volume strain as a function of pressure held together least well, despite a higher green fractional density.

4.3. Triaxial compression

Representative, complete stress-strain curves for the 94% and 99.5% alumina powders are presented in Fig. 4. Summary plots of *all* of the triaxial compression experiments on the 94% and 99.5% alumina powders are presented in Fig. 5. In the latter, $\sigma_1 - \sigma_3$ is plotted versus axial strain (ε_a), omitting the lateral and volume strains for the sake of clarity. In both figures, the periodic drops in stress difference mark the points at which the specimens were unloaded and reloaded to measure Young's modulus and Poisson's ratio.

From Figs 4 and 5, it is clear that the two powders have much in common. Neither of the powders shows a clear "yield point" at any confining pressure, and both powders exhibit nonlinear behavior from the outset, hardening continuously with deformation. Additionally, both powders undergo an extended period of shear-enhanced compaction concurrent with deviatoric loading [16–18], as indicated by the steady increase in volume strain (Fig. 4). Inevitably, the compaction stage is followed by a reversal of the volume strain behavior

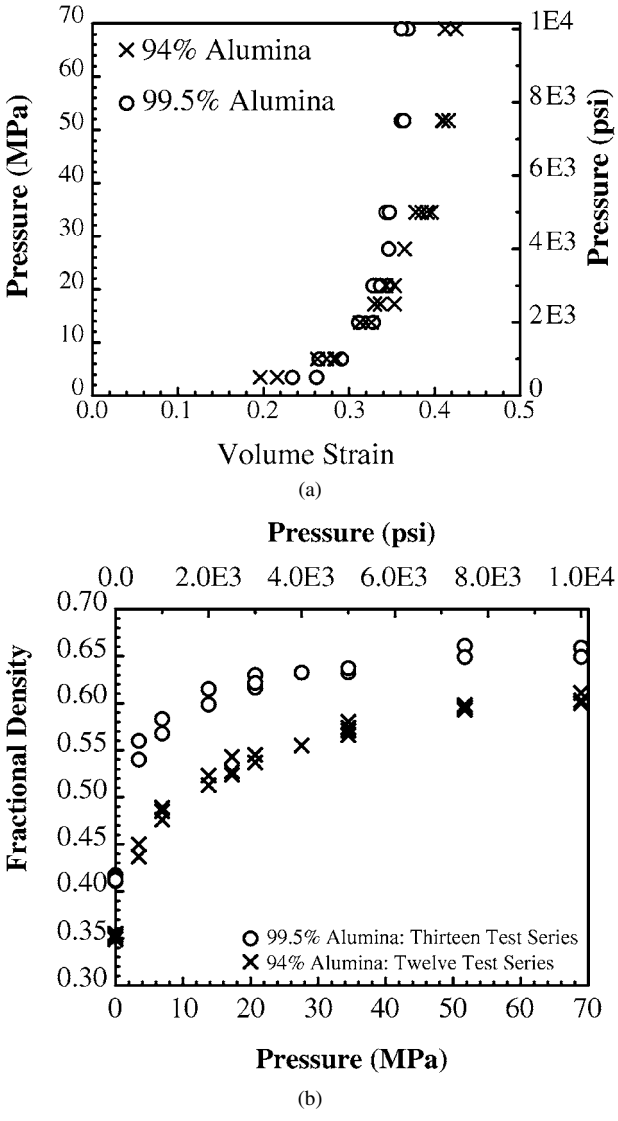

Figure 3 Plots of (a) pressure-volume strain and (b) fractional density-pressure relationships for the two green alumina powders.

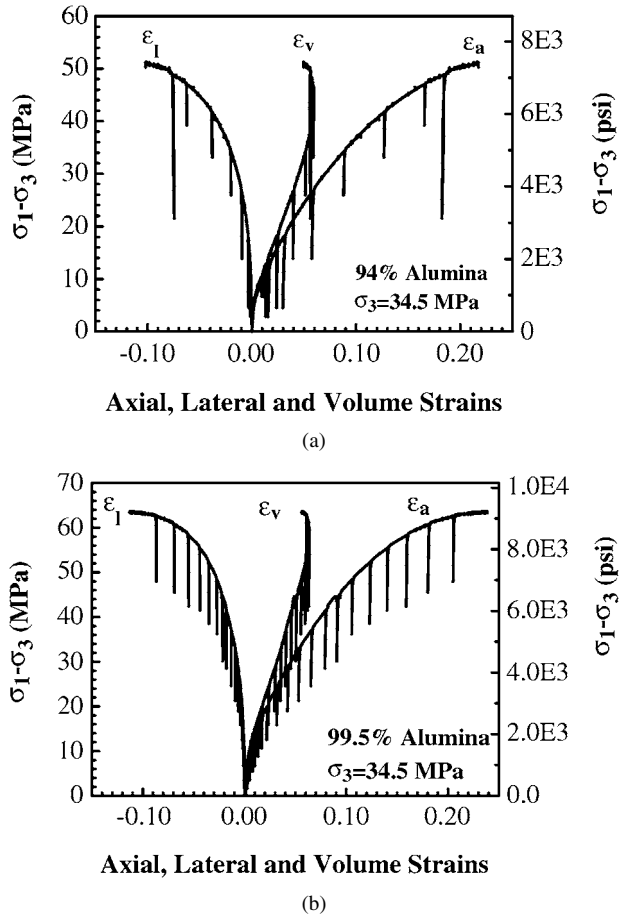

Figure 4 Representative plots of axial (ε_a), lateral (ε_l) and volume (ε_v) strain as a function of differential stress for (a) 94% alumina, and (b) 99.5% alumina powder compacts tested using an axial strain rate of 10^{-4} s^{-1} and a confining pressure of $\sigma_3 = 34.5$ MPa (5000 psi). The periodic drops in stress difference mark the points at which the specimens were unloaded and reloaded to measure Young's modulus and Poisson's ratio.

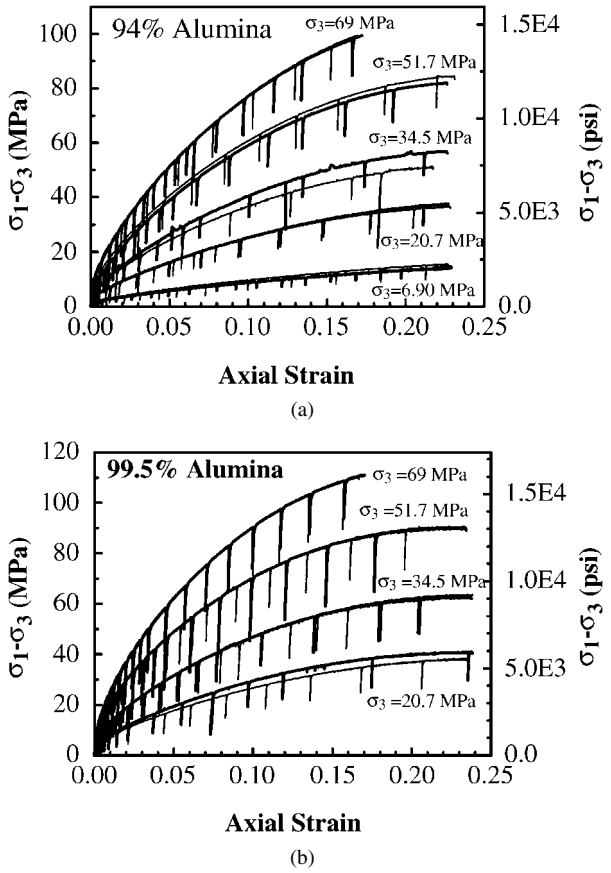

Figure 5 Summary plots of axial strain as a function of differential stress for the different confining pressures used in the triaxial experiments completed on the (a) 94% and (b) 99.5% alumina powders using an axial strain rate of 10^{-4} s^{-1}. The periodic drops in stress difference mark the points at which the specimens were unloaded and reloaded to measure Young's modulus and Poisson's ratio. Note the increase in shear strength with confining pressure, σ_3, and the absence of a clear yield point at any pressure.

starting at axial strains of about 0.10–0.15. This reversal in volume strain marks the onset of increasing specimen volume, or dilatancy [11–13, 16–18]. For soils and other granular materials, the onset of dilatant behavior is usually taken to indicate that particles have been packed together as closely as possible, and have now begun to shear past one another, causing a net increase in volume [11, 13].

The rate of hardening continuously decreases with increasing pressure, and with the exception of the experiments performed at $\sigma_3 = 69$ MPa (10,000 psi), the plots of axial strain as a function of stress difference are almost flat at axial strains greater than 0.20 (Fig. 5). At no point do the specimens completely "fail" (i.e., lose all load-bearing capability) in triaxial compression. Consequently, we have taken the onset of specimen failure—or, more accurately, "yield"—to occur at the point at which the volume strain plot completely reverses direction (Fig. 4). This reversal corresponds to a definite physical event, namely the point at which shear deformation clearly dominates volumetric (i.e., compactive) deformation. The reversal point can be chosen unambiguously, and, in all but two of our experiments a *full* reversal is exhibited. In the two exceptions, the volumetric strain was starting to reverse, but did not fully do so. We take the stresses at which we define yield to occur also to define our failure surface.

The shear strength of both powders increases steadily with increasing confining pressure, σ_3 (Fig. 5). This is simply a consequence of the increasing interlocking of individual particles with increasing compaction [11–13]. Interestingly, the 99.5% alumina powder is significantly stronger in shear than the 94% alumina powder under all conditions. This difference in shear strength marks a clear distinction between the mechanical behaviors of the two powders.

4.4. Elastic moduli and Poisson's ratio

Bulk moduli were measured as a function of forming pressure at the beginning of every triaxial compression experiment. The results for both powders are summarized in Fig. 6. In general, bulk modulus increases approximately linearly with pressure, with the 99.5% alumina powder consistently having the higher modulus. Interestingly, while it would be expected that the bulk modulus would eventually asymptote to a near-constant value, this has not happened within the pressure range studied. Note that, in contrast to the measurements of Young's modulus and Poisson's ratio, bulk modulus was measured only at the beginning of the triaxial test.

Young's modulus was measured repeatedly during the course of the triaxial compression experiments (Figs 4 and 5). Young's moduli for the *first* unloading-reloading cycle in each triaxial test are presented in Fig. 7 for the two alumina powders. Like the bulk modulus, Young's modulus appears to increase approximately linearly with pressure up to 68.9 MPa (10,000 psi). There is a slight suggestion at 68.9 MPa that limiting values are being approached; however, more data at higher pressures would be required to confirm this. Also, as observed for bulk modulus, the 99.5% alumina powder exhibits consistently higher values for E than the 94% alumina powder.

For both powders, Young's modulus increases steadily with axial and volumetric strain. As such, the moduli measured at the end of the experiment are typically greater by a factor of two to three. These increases in E might be expected owing to the increased compaction, and, hence, particle interlocking, that occurs

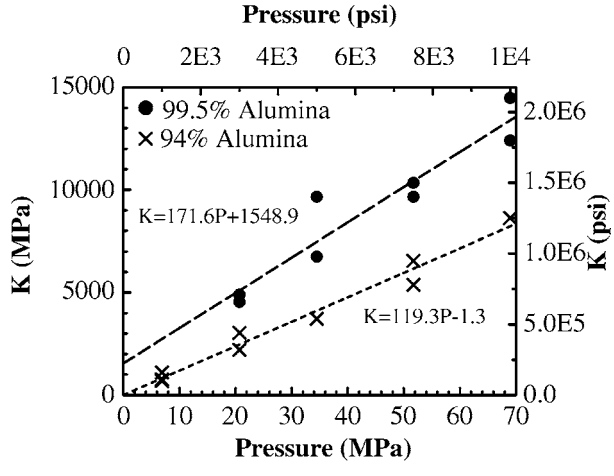

Figure 6 Bulk modulus, K, measured as a function of forming pressure (and compact density per Fig. 3) for the 94% and 99.5% alumina powders, including linear "best fits" to the data.

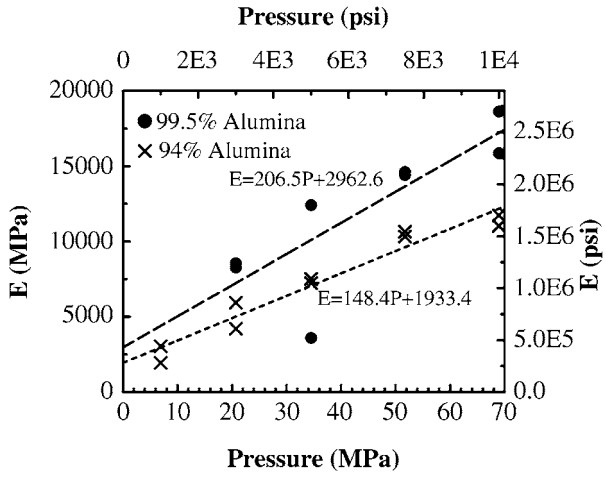

Figure 7 Young's modulus, E, measured as a function of forming pressure (and compact density per Fig. 3) for the 94% and 99.5% alumina powders, including linear "best fits" to the data.

during deviatoric loading; however, E usually continues to increase even in the latest stages of the experiments when dilation occurs and the volume is *increasing*. It is not clear why this should be so. Assuming that at least some of the apparent increase in E may be a consequence of growing uncertainty in the cross-sectional area as a result of inhomogeneous deformation, the measurements made earliest in the experiments are probably the most reliable.

Measurements of Poisson's ratio, (ν) were made simultaneously with those of Young's modulus, using the same unloading-reloading loops shown in Figs 4 and 5. Values of ν determined from the first load cycle in each experiment are plotted versus forming pressure in Fig. 8. Although scatter is quite large, values for the 94% alumina powder generally fall in the range of 0.2–0.3. These values are considerably greater than the values for the 99.5% alumina, which initially, and

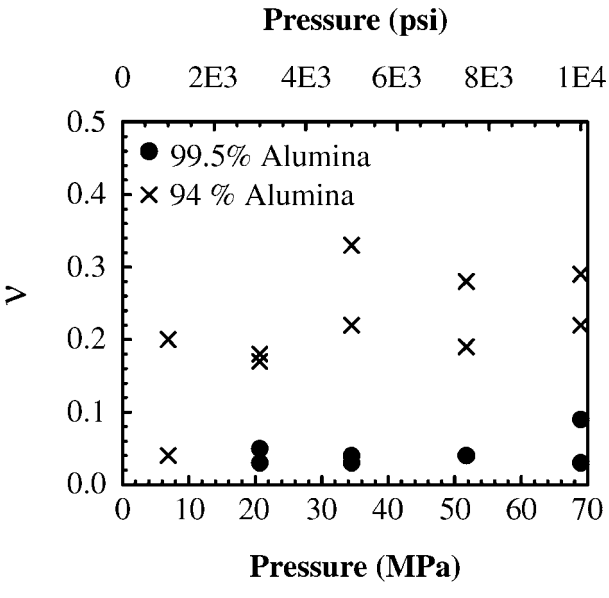

Figure 8 Poisson's ratio, ν, measured as a function of forming pressure (and compact density per Fig. 3) for the 94% and 99.5% alumina powders. Note the general insensitivity of ν to pressure in contrast to the elastic moduli presented in Figs 6 and 7.

quite consistently, are in the range of 0.02–0.04. This difference indicates a very large difference in the ability of the 99.5% alumina to transmit load compared to the 94% alumina powder. Interestingly, Poisson's ratio appears to be quite insensitive to pressure, in contrast to the bulk modulus and Young's modulus. The reason for this is not known.

As observed for Young's modulus, Poisson's ratio increases steadily during the course of a triaxial deformation experiment. In the case of the 94% alumina powder, the values typically reach 0.4–0.5 by the conclusion of the test, without any consistent relationship to confining pressure. For the 99.5% alumina powder, values at the conclusion of the triaxial experiments were in the range of 0.2–0.4, again, without any consistent relationship to the confining pressure. One might expect Poisson's ratio to increase during an experiment because all specimens undergo a period of compaction during triaxial deformation: like Young's modulus, Poisson's ratio would increase as particle interlocking, and, hence, load transmissivity in the specimen, increases. However, unlike the various elastic moduli, we have noted that the Poisson's ratio first measured during each triaxial experiment is relatively insensitive to forming pressure, and, hence, density over the pressure range of our investigation. Since we do not see a consistent increase of Poisson's ratio with forming pressure, it is not clear why it should increase so greatly with deformation in the course of a single experiment.

Poisson's ratio tends to increase most rapidly in the late stages of the experiments, in two instances reaching unreasonably high values of 0.6 and 0.97. However, because such high values are measured only in the final stages of the experiments, we believe that they are spurious, reflecting: (1) increasingly inhomogeneous deformation; and (2) plastic—not elastic—processes. With regard to (1), specimen barreling increases throughout the experiments, and reflects an increasing concentration of deformation in the center of the specimens. True axial and lateral strains become less and less certain, and, consequently, so do values for ν. Indeed, this increasingly less homogeneous deformation may explain the increase of ν with strain in all of the experiments, despite the seeming density-independence of ν. With respect to (2), the specimens are dilating rapidly in that final stages of the experiments. This most likely means that a large number of granules are now shearing past one another and/or fracturing, causing the volume to increase. Although the purpose of the unload/reload cycles is to capture the elastic response of the interlocked particles, it is possible that, when dilation dominates, even the unload/reload cycles are dominated by plastic deformation processes at the microscopic scale. That is, it is assumed that upon unloading and reloading, particles remain interlocked and motionless, yielding a true elastic modulus until the previous load is exceeded. It is possible that once dilation begins this assumption no longer holds: plastic processes at the granule scale may result in unusually large lateral strains and correspondingly large values for ν. If, however, these large values are attributable in some measure to plastic processes, then, strictly speaking, they should not be referred to as

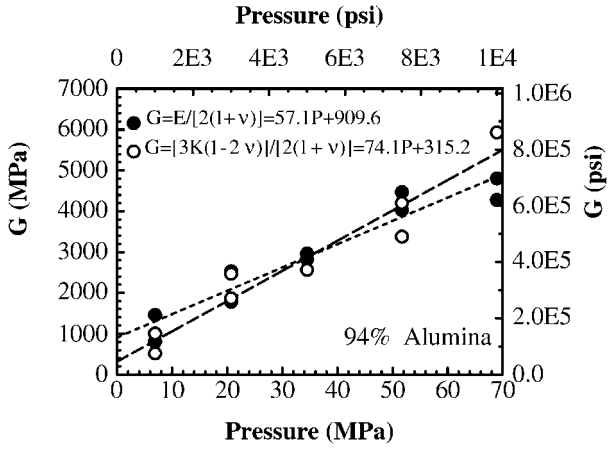

(a)

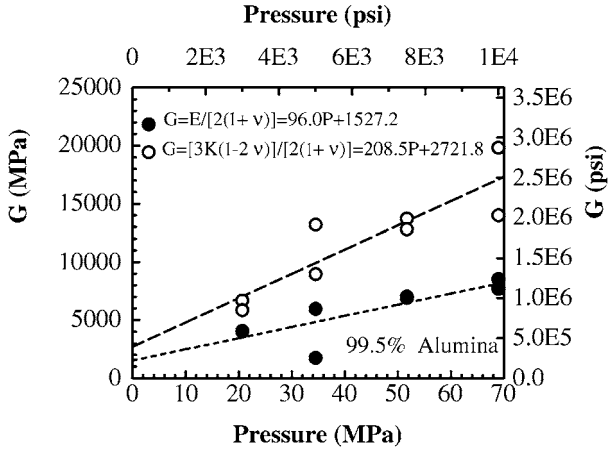

(b)

Figure 9 Shear modulus, G, calculated for the (a) 94% and (b) 99.5% alumina powder as a function of forming pressure (and compact density per Fig. 3) using the two different sets of experimentally measured parameters as shown. Best linear fits to both calculated results are also shown.

"Poisson's ratio." ν is an elastic constant, and we may no longer be in the "elastic" regime.

With values for K, E, and ν in hand, and assuming material isotropy, the shear modulus, G, can be calculated. As a check of the consistency of our measurements and the credibility of our results, G was calculated in two different ways [19] from the experimentally determined properties. The results for both powders are presented in Fig. 9. Agreement between the two calculations is inarguably excellent for the 94% alumina powder (Fig. 9a). Agreement between the two calculations for the 99.5% alumina powder is comparatively less good (Fig. 9b); however, the linear fits to the moduli never disagree by more than a factor of 2.5 over the entire range of our measurements. In fact, G can be calculated a third way, directly from K and E [19, p. 80]. Results from this third calculation agree closely with the calculation using E and ν and, so, are not shown. Given the necessary complexity of our experimental procedure and its inherent, and occasionally imponderable uncertainties, we take this result as confirmation of the overall reasonableness of our approach.

Although there is insufficient data to make a quantitative assessment, the measured differences in the mechanical properties between the two alumina powders examined may be attributable to some of the physical characteristic differences summarized in Table I. In particular, the higher moduli measured for the 99.5% alumina powder could be related to its finer particle size. Simple tests conducted in our laboratories involved characterizing different primary particle size alumina powders (i.e., otherwise nominally identical) compacted to equivalent fractional densities by die pressing. Finer particles produced stronger (i.e., in tension) compacts, which would be consistent with higher moduli. Likewise, it would be reasonable to assume that a higher binder content could contribute to a higher tensile strength compact, and perhaps higher moduli.

The relatively large difference in Poisson's ratio measured for the two alumina powders indicates that there is a very large difference in the ability of the 99.5% alumina to transmit load compared to the 94% alumina powder. This too may be related to particle size. In FEM compaction model simulations using the modeling parameters for pure alumina reported by Aydin *et al.* [2] and the parameters measured for the 94% alumina in this study, transmission of the load was much better in the coarser particle size 94% alumina. This was true despite the fact that similar values of Poisson's ratio were used in both simulations. The predicted inability of the finer particle size alumina powder to transmit load as efficiently would be consistent with a lower measured Poisson's ratio.

4.5. Shear failure surfaces and estimation of the cap shape and evolution

As noted earlier, shear failure in our triaxial compression experiments has been defined as the point at which the volume strain curve totally reverses from compaction to dilatation. The loci of these points in stress difference-confining pressure space thus defines the shear failure surface. These surfaces are plotted in Fig. 10 for the two powders, but in $\sqrt{J_2'} - \sigma_m$ space to be consistent with the analysis of Aydin *et al.* [2]. Here, $\sqrt{J_2'}$ is the square root of the second invariant of the deviatoric stress, and σ_m is the mean stress. In our test geometry, these quantities correspond to $(\sigma_1 - \sigma_3)/\sqrt{3}$ and $(\sigma_1 + 2\sigma_3)/3$, respectively [2]. The shear failure surfaces for both powders are clearly linear under the conditions of this study. The slopes of the lines that we have fitted to the data correspond to $\tan\beta$, where β is the angle of internal friction. The linear shear failure surface intercepts the abscissa at d, which defines the cohesion of the material.

The shear failure surface constitutes one of the two critical elements of the Drucker-Prager cap model employed by Aydin and co-workers to model powder compaction [2]. The other element is a curved "cap" that intersects both the mean stress axis and the shear failure surface (Fig. 1). Deformation is elastic within the wedge-shaped region defined by the cap, the mean stress axis, and the shear failure surface. Loading that intersects the shear failure surface results in failure by shear slip. Hydrostatic loading along the mean stress axis that intersects the cap results in permanent volumetric deformation. Loading paths that intersect the

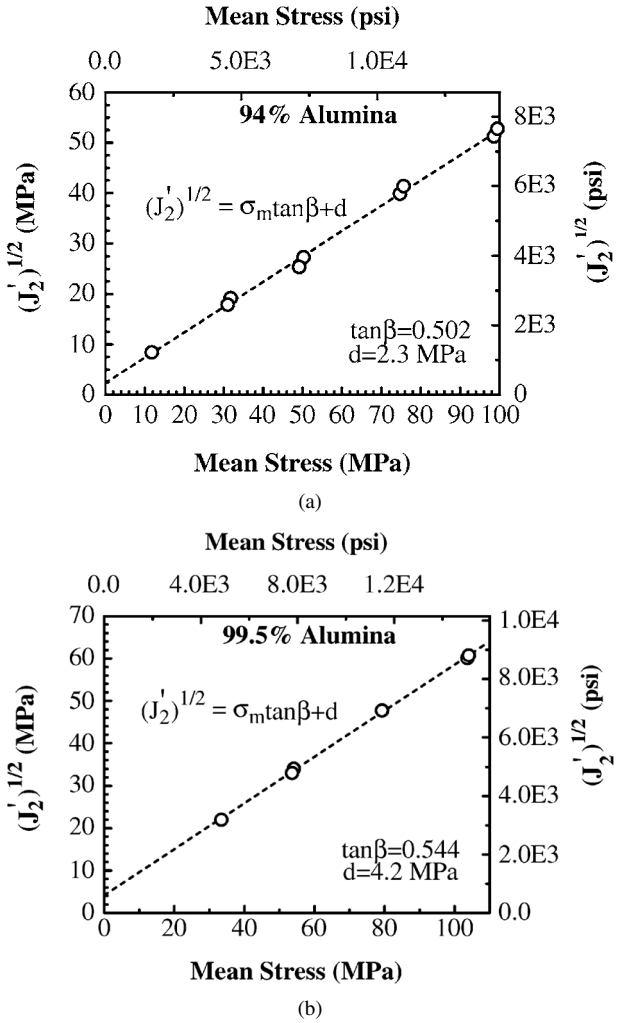

Figure 10 The shear failure surfaces, represented by a line of slope tan β and intercept d, for the (a) 94% and (b) 99.5% alumina powders, respectively.

cap other than where it intercepts the mean stress axis or shear failure surface results in both permanent shear and volumetric strains.

The cap is moveable, consistent with the experimentally observed history-dependence of the mechanical properties of soils, porous rock, and other granular media such as ceramic powders. That is, increasing the mean stress without intercepting the failure surface continuously pushes the cap outward to the right, between the shear failure surface and the mean stress axis. The material becomes *hardened*, and upon unloading, the region of elastic deformation is irreversibly expanded. In the Drucker-Prager cap model, the shear failure surface is linear and fixed. However, some models include nonlinear (e.g., Argüello *et al.* [5]) and/or hardening [14] shear failure surfaces, too.

Though the main focus of this paper has been on measurement of the mechanical properties of ceramic powders, it is nevertheless of interest to see if information can be extracted about the shape and movement of the cap in terms of the same Drucker-Prager cap model used by Aydin *et al.* [2]. To this end, a method was devised to extract the relevant data from the hydrostatic and triaxial compression experiments in this study, and fit them to Aydin and co-workers' Equations 5 and 6 [2] that define the shape and hardening of the cap. The procedure is outlined in detail for the 94% alumina powder, and then compared to the results from a similar analysis of the 99.5% alumina powder.

Rewritten using only slightly different nomenclature, the relevant equations are:

$$F_c = \left\{ (\sigma_m - P_a)^2 + \left[\frac{R\sqrt{J_2'}}{\left(1 + \alpha - \left(\frac{\alpha}{\cos\beta}\right)\right)} \right]^2 \right\}^{\frac{1}{2}} - R(d + P_a \tan\beta) = 0 \quad (1)$$

where,

$$P_a = \frac{P_b - Rd}{(1 + R\tan\beta)} \quad (2)$$

In Equation 1, F_c is the function describing the elliptically-shaped cap, P_a is the cap evolution parameter, R is the cap shape parameter, α is an additional cap shape parameter that smoothes the transition between the shear failure surface and the cap, and σ_m, $\sqrt{J_2'}$, d, and β have been defined previously. The cap evolution parameter, P_a, represents the increase in elastic strength that occurs with permanent, plastic, volumetric strain. P_a is related to the volumetric plastic strain, ε_v, through the hydrostatic compaction yield strength, P_b, in Equation 2. The functional relationship between P_b and ε_v is precisely what we determined in our hydrostatic compaction experiments to obtain the pressure-density relationships illustrated in Fig. 3.

In Fig. 11, the results of the hydrostatic compaction experiments on the 94% alumina powder are re-plotted as pressure versus volume strain, and the data was fitted with an equation having the form

$$P_b = A \exp(B\varepsilon_v). \quad (3)$$

With the information provided in Figs 11 and 12 and the data from the triaxial compression experiments on

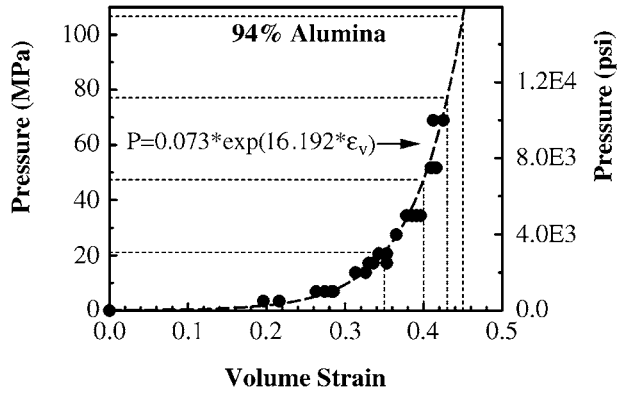

Figure 11 Pressure-volume strain plot of data from the hydrostatic compression experiments on the 94% alumina powder. Fine dashed lines illustrate the manner in which values for P_b are determined for selected values of plastic volume strain. The equation fitted to the data is shown as the bold, dashed line.

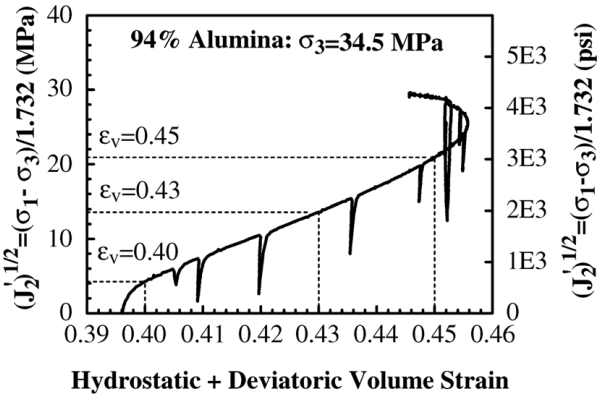

Figure 12 An example from a triaxial compression experiment on 94% alumina powder illustrating the manner in which values of $\sqrt{J_2'}$ are determined for three of the four selected plastic volume strains shown in Fig. 11 ($\varepsilon_v = 0.40$, 0.43 and 0.45). Note that this particular specimen compacted to a volume strain of about 0.396 under hydrostatic compression alone, so there is no value of $\sqrt{J_2'}$ corresponding to $\varepsilon_v = 0.35$ for this particular test.

the 94% alumina powder, both the shape and movement of the cap can be examined.

The analysis first involves selecting a limited number of specific volume strains to examine from the hydrostatic and triaxial compression experiments, being particularly careful to select a set that is well represented within the range of *total* volume strains that were attained during the triaxial deformation experiments. These values are obtained by simply adding the final volume strains from the hydrostatic compression experiments to the strains accumulated during the triaxial tests.

In our case, we selected specific volume strains of $\varepsilon_v = 0.35$, 0.40, 0.43, and 0.45. Then, using Fig. 11, we determined (by calculation or visually) the hydrostatic yield pressures, P_b, that correspond to each of these four volume strains. Similarly, on a plot of $\sqrt{J_2'}$ versus total volume strain from the triaxial compression experiments (Fig. 12), we determined the corresponding values of $\sqrt{J_2'}$. (Note that, in principle, one should subtract out the elastic component of the volume strain before making this correspondence; however, the elastic strain is a relatively small component of the total strain in our experiments.) Knowing the confining pressures at which the experiments were conducted, we then calculated the corresponding values of the mean stresses at which the particular volume strains were attained. In this way, we obtained four separate tables of combinations of $\sqrt{J_2'}$, σ_m and P_b, each of which corresponds to one of the four values of ε_v that we chose.

These four data sets are plotted in Fig. 13 along with the shear failure surface for the 94% alumina powder to obtain a semi-quantitative picture of the movement of the cap with volumetric strain. Although the scatter in the data is fairly large, it is clear that the cap moves to the right with increasing ε_v and P_b.

The shape of the cap cannot be uniquely determined from the data; however, we did fit Equations 1 and 2 to the data to see if a single set of self-similar ellipses could reasonably describe the data. This was accomplished by substituting Equation 2 into 1, yielding a single equation in which d and β are known. Then with the experimental data for $\sqrt{J_2'}$, σ_m and P_b, the best-

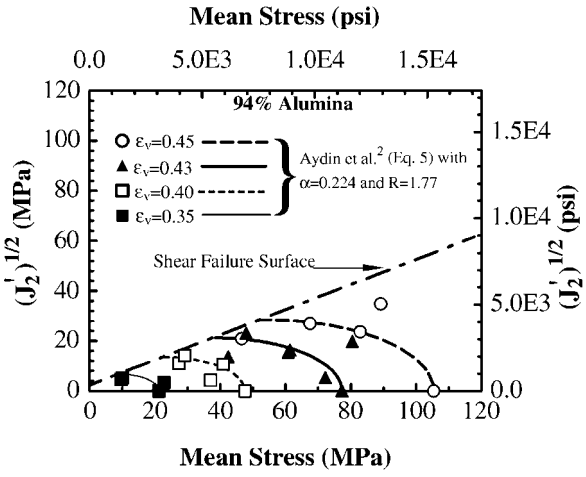

Figure 13 Plot of the $\sqrt{J_2'} - \sigma_m$ pairs for the four selected values of plastic volume strain for the 94% alumina powder. Each set corresponding to a particular volume strain is identified by a separate symbol. The shape and evolution of the cap is explored by "contouring" these sets of points with a cap of the form used by Aydin *et al*. [2] fitted to the data. Note that the cap must move to the right with increasing mean stress and, hence, plastic volume strain. Although scatter in the data does not require an elliptical cap, that form is consistent with the data.

fitting values for R and α were calculated. Values of $R = 1.81$ and $\alpha = 0.224$ were determined for the 94% alumina powder, with a correlation coefficient of 0.72. The resulting ellipses for the four values of ε_v and P_b are also plotted in Fig. 13. Clearly, a single set of ellipses could reasonably describe the data.

A similar exercise was performed with the data for the 99.5% alumina powder, producing somewhat different results. Owing to the stiffer volumetric strain response of the 99.5 alumina powder, we had a smaller overall range of volumetric strain from which to select specific values, which included $\varepsilon_v = 0.35$, 0.37, 0.39 and 0.41. These points of constant volumetric strain are plotted in $\sqrt{J_2'} - \sigma_m$ space in Fig. 14, along with the shear failure

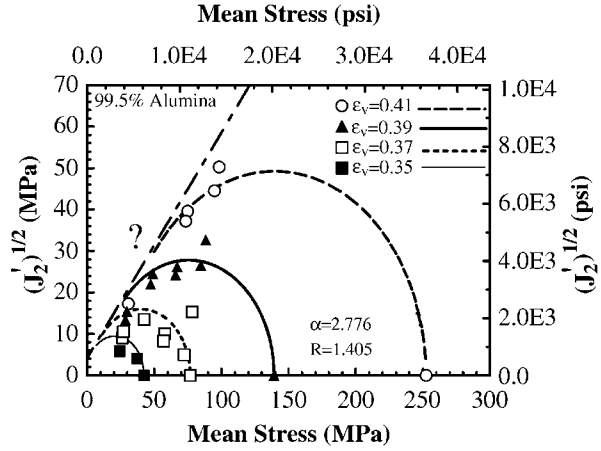

Figure 14 Plot of the $\sqrt{J_2'} - \sigma_m$ pairs for the four selected values of plastic volume strain for the 99.5% alumina powder. Each set corresponding to a particular volume strain is identified by a separate symbol. The shape and evolution of the cap is explored by "contouring" these sets of points with a cap of the form used by Aydin *et al*. [2] fitted to the data. Note that the cap must move to the right with increasing mean stress and, hence, plastic volume strain. Note also that the tight clustering of points for all four volume strains at the left of the plot requires a much more "tangential" approach of the cap to the shear failure surface (solid line) than does the data for the 94% alumina in Fig. 13. The question mark (?) indicates our uncertainty that the ellipses plotted constitute at "best fit" to these data.

surface for the 99.5% alumina powder. It is clear that the surfaces of constant volume strain move outward and to the right; however, the shape of the cap defined by these contours must be somewhat different than that for the 94% alumina powder.

Following the $\varepsilon_v = 0.35$, 0.37, 0.39 or 0.41 contours from left to right, the data clearly require a rise in the contours before descending to intersect the mean stress axis. This in turn requires a near-tangential approach of the cap to the shear failure surface at the left ends of the contours, quite unlike the results for the 94% alumina powder (Fig. 13). Thus, if the cap is elliptically shaped as required by the Drucker-Prager cap-plasticity model, the cap must evolve approximately as shown in Fig. 14, with $\alpha \cong 2.776$ and $R \cong 1.405$. We say "approximately" because efforts to fit Equations 1 and 2 to the data for the 99.5% alumina were not altogether satisfactory. Despite a high correlation coefficient (0.98), the resulting family of ellipses failed to fully intersect the shear failure surface as mathematically required. This may represent a numerical problem with our fitting routine, or, more fundamentally, indicate that the Drucker-Prager cap model does not adequately describe the 99.5% alumina powder. Despite our inability to obtain a totally convincing fit, nothing mathematically or physically excludes a cap shape such as that shown in Fig. 14.

4.6. Analysis of materials parameters for modeling

Using a very different experimental approach, we *directly* measured the same material parameters that Aydin and co-workers [2] indirectly determined, or estimated, for an agglomerated alumina powder. A comparison of the results from this study with those of Aydin *et al*. [2] reveals generally good agreement between the two (Table II), confirming both the specific numbers that they obtained, and the applicability of the numerical model that they employed. However, the results from this study offer some possible refinements to the materials parameter data used by Aydin *et al*. [2] in their modeling analysis and, perhaps, some additional insight into the discrepancies between their model predictions and experimental observations.

TABLE II Summary of the properties of the two alumina powders characterized in this study compared to the alumina properties reported by Aydin *et al*. [2]. Values of K, G and E for 94% and 99.5% alumina at 34.5 MPa (5000 psi) were calculated from the linear least-squares fits given in Figs 6, 7 and 9

Property	94% Alumina (at $\sigma_3 = 34.5$ MPa)	99.5% Alumina (at $\sigma_3 = 34.5$ MPa)	Alumina [2]
K (MPa)	4115	7469	6777.4
G (MPa)	2880	7377	3531.9
E (MPa)	7053	10,087	9027.4
ν	0.28	0.04	0.278
β	26.7°	28.5°	16.5°
d (MPa)	2.3	4.2	5.5
R	1.77	1.405	0.558
α	0.224	2.776	0.03

From a single die-pressing experiment to a pressure of 89.6 MPa (13,000 psi) Aydin *et al*. [2] obtained values of 6,777 MPa (9.8×10^5 psi), 3,531 MPa (5.1×10^5 psi), and 9,027 MPa (1.3×10^6 psi) for K, G and E respectively. These values fall roughly in middle of the ranges that were measured for the two different agglomerated alumina powders examined in this study, and therefore probably represent reasonable averages. Nevertheless, the moduli are clearly pressure- (and possibly strain-) dependent, and differ from powder to powder.

Aydin *et al*. [2] estimated Poisson's ratio for their powder from the literature as 0.278. This value is consistent with the results for one of the alumina powders characterized (0.2–0.3), but very different from the other (0.02–0.04). The reason for this difference is not known, but an order of magnitude difference in ν might be expected to have a significant impact on model-based predictions of densities and density gradients. Our results further suggest that ν is relatively insensitive to pressure, but may be sensitive to strain.

Our measurements indicate that the shear failure surface is very linear up to 68.9 MPa (10,000 psi) for both the 94% and 99.5% alumina powders, consistent with Aydin and co-workers' selection of the Drucker-Prager cap model. Their estimates of $d = 5.5$ MPa (798 psi) and $\beta = 16.5°$ are not that different from our values of $d = 2.3$ MPa (340.6 psi) and $\beta = 26.7°$ for the 94% alumina powder, and $d = 4.2$ MPa (605.2 psi) and $\beta = 28.5°$ for the 99.5% alumina powder.

Interestingly, Aydin *et al*. [2] suggested that some of the discrepancies that they reported between density gradients predicted using their numerical model and the gradients they observed in their die-pressing experiment might be attributable to a pressure-dependent angle of internal friction and/or material cohesion. If this were the case, the shear failure envelope would be nonlinear. Although we have not fully investigated the same pressure region as Aydin *et al*. [2] (89.6 MPa = 13,000 psi) our results indicate that these quantities are constant to at least 68.9 MPa (10,000 psi). It appears likely that the discrepancies between model and experiment that were reported by Aydin and co-workers have to be attributed to other phenomena, such as a pressure-dependent die wall friction coefficient [2], a different value for Poisson's ratio, pressure-dependent elastic properties, or some combination thereof.

4.7. Experimental modifications

The results from this study can be used to infer something about both the shape and evolution of the cap that describes expansion of the elastic region with volumetric strain. The data are consistent with an elliptically-shaped cap. However, our results do not prove that the cap is elliptical in shape. We can refine our understanding of the shape of the cap only by performing a series of triaxial experiments on deliberately "over-hardened" specimens; that is, specimens that have been first hydrostatically compressed to higher pressures than those at which the triaxial stage tests are performed. In this way, we could choose loading paths that intersect the cap off of the mean stress axis. This process is tedious,

but is the only sure way to map out the structure and evolution of the cap; indeed, such a process is the only method by which to confirm the *existence* of a cap.

Improving the sample strain and property measurements represent other areas of interest. Our existing test configuration should allow us to use more than one transverse LVDT, improving our estimate of the change in sample cross-sectional area with deformation. Additionally our test configuration should also allow endcap-to-endcap acoustic velocity measurements during the triaxial compression experiments, which would allow independent confirmation of the change in elastic parameters with strain.

The last major area that needs to be addressed to characterize powders and compaction behavior involves designing an undrained test (i.e., a test in which the gases within the pore spaces of the particulate body are not allowed to escape freely during compaction). All of our experiments have been conducted in the drained configuration.The undrained configuration represents the opposite extreme, and may be more representative of some industrial processes. The same porous, pressure-sensitive material can exhibit very different mechanical properties under the two different conditions.

5. Summary

Representative numerical simulations of powder compaction require accurate material properties and realistic constitutive laws. An essential part of the work described herein has been to directly measure as many of the requisite powder properties as possible to model powder compaction using a modified Drucker-Prager cap-plasticity model. This has entailed taking a soil mechanics approach to the measurements, which, though being direct, turns out not to be particularly simple. Owing to the large strains that are associated with loosely packed ceramic powders, we have developed a two-stage process in which we first determine the pressure-density relationships for the powders in hydrostatic compression, and subsequently test precompacted specimens under deviatoric loading conditions. The properties that we have determined directly using this method include the seven parameters that are required for application of the modified Drucker-Prager (or Sandler-Rubin) cap-plasticity models. Additionally, we have determined pressure-density relationships for our test materials. Using a somewhat more indirect route, we also have used the foregoing data to infer something about the shape of the cap, and the manner in which it moves with increasing mean stress.

We determined the materials properties of two different alumina powders up to a compaction pressure of 68.9 MPa (10,000 psi). While detectable mechanical differences do exist between the two different powders, there are some consistent general trends as well. The various elastic moduli are both pressure and strain dependent. Poisson's ratio appears to be relatively insensitive to pressure, but does evolve as a function of strain. The failure surface and cohesion appear to be quite linear (i.e., β is a constant) up to 68.9 MPa (10,000 psi).

The modeling parameters determined and estimated by Aydin *et al*. [2] are generally consistent with the values measured in this study; however, this work provides added insight into their dependence on pressure and fractional density (or volume strain). The various elastic moduli and Poisson's ratio for the alumina powder studied by Aydin *et al*. fall within the range of those that we have measured; however, Aydin and co-workers took these elastic properties to be constants. In fact, they are pressure dependent. Additionally, our results show that the failure surface and cohesion appear to be quite linear parameters, in contrast to what Aydin *et al*. [2] surmised might not be constant in order to explain differences between predicted and observed densities in powder.

Probing the shape and structure of the caps for the two powders studied constitute one area in which we plan further work using the existing experimental technique. Another important objective will be to link the differences in properties of different powders to specific powder characteristics (e.g., grain/agglomerate size and/or shape, surface area, and binder properties and content).

Acknowledgements

We are indebted to William A. Olsson for helpful discussions on many aspects of cap-plasticity models. We are particularly grateful for his outline of the technique by which information about the shape and movement of the caps could be extracted from our data. We also thank AACCMCI, Inc., William Blumenthal of Los Alamos National Laboratory, Robert Lagasse of Sandia National Laboratories, and Julie Anderson of the University of New Mexico for providing materials and materials property data that contributed to this study. Finally, we thank Donald Ellerby and William A. Olsson of Sandia National Laboratories for providing critical reviews of this manuscript in preparation for publication. This work was supported by the U. S. Department of Energy under Contract DE-AC04-94AL85000, and by AMMPEC, Inc. through a DOC/EDA Grant. Sandia is a multiprogram laboratory operated by Sandia Corporation, a Lockheed Martin Company.

References

1. I. AYDIN, B. J. BRISCOE and K. Y. SANLITURK, *Comput. Mater. Sci.* **3** (1994) 55.
2. *Idem.*, *Powder Tech.* **89** (1996) 239.
3. O. COUBE, Ph.D. thesis, University Pierre et Marie Curie, Paris VI, March 1998.
4. J. M. KELLER, J. D. FRENCH, B. DINGER, M. McDONNOUGH, B. GOLD, C. CLOUTIER, L. CARINCI, E. VAN HORN, K. EWSUK and B. BLUMENTHAL, *American Ceramic Society Bulletin* **77**(10) (1998) 52.
5. J. G. ARGÜELLO, K. G. EWSUK, D. H. ZEUCH and A. F. FOSSUM, in 49th Pacific Coast Regional and Basic Science Division Meeting of the American Ceramic Society, San Francisco, October 12–15, 1997.
6. J. G. ARGÜELLO, D. H. ZEUCH, A. F. FOSSUM and K. G. EWSUK, *KONA*, in press.
7. L. HUANG and V. M. PURI, in "Fine Powder Processing Technology," edited by R. Hogg, R. G. Cornwall, and C. C. Huang, p. 361, Proc. Fine Powder Processing Conf., Pennsylvania State University, University Park, PA, Sept. 1997.

8. *Idem.*, in ASAE 1998 Annual International Meeting, Orlando, FL, July 12–16, 1998 (American Society of Agricultural Engineers, MI, USA) Paper No. 984022.
9. D.-Z. SUN and H. RIEDEL, in "Simulation of Materials Processing: Theory, Methods and Applications," edited by S.-F. Shen and P. R. Dawson, p. 881, Proc. Fifth International Conference on Numerical Methods in Industrial Forming Processes, Ithaca, NY, June 18–21, Balkema, Rotterdam, 1995.
10. X.-K. SUN, K.-T. KIM and G.-D. WANG, *J. Amer. Ceram. Soc.* **81**(12) (1998) 3318.
11. M. S. PATERSON, "Rock Deformation: The Brittle Field" (Springer-Verlag, New York, 1978).
12. J. C. JAEGER and N. G. W. COOK, "Fundamentals of Rock Mechanics," 2nd ed. (John Wiley and Sons, New York, 1976).
13. T. W. LAMBE and R. V. WHITMAN, "Soil Mechanics" (John Wiley and Sons, New York, 1969).
14. I. S. SANDLER, F. L. DIMAGGIO and G. Y. BALADI, *J. Geotech. Eng. Div. ASCE* **102** (1976) 683.
15. R. D. HARDY, Rept. No. SAND93-0256, Sandia National Laboratories, Albuquerque, NM, 1993.
16. R. N. SCHOCK, H. C. HEARD and D. R. STEPHENS, *J. Geophys. Res.* **78** (1973) 5922.
17. J. N. JOHNSON and S. J. GREEN, in "The Effects of Voids on Material Deformation" edited by S. C. Cowin and M. M. Carrol (The American Society of Mechanical Engineers, New York, 1976) p. 93.
18. T.-F. WONG, H. SZETO and J. ZHANG, *Appl. Mech. Rev.* **45**(8) (1992) 281.
19. F. A. MCCLINTOCK and A. S. ARGON, "Mechanical Behavior of Materials" (Addison- Wesley, Reading, MA, 1966).

Received 26 May
and accepted 26 December 2000